

Satellite based fault diagnosis of photovoltaic systems using recurrent neural networks

Jonas Van Gompel*, Domenico Spina, Chris Develder

IDLab, Department of Information Technology, Ghent University - imec, Technologiepark-Zwijnaarde 126, 9052, Ghent, Belgium.

Abstract

Due to manufacturing defects and wear, faults in photovoltaic (PV) systems are often unavoidable. The effects range from energy losses to risk of fire and electrical shock, making early fault detection and identification crucial. Literature focuses on PV fault diagnosis using dedicated on-site sensors or high-frequency current and voltage measurements. Although these existing techniques are accurate, they are not economical for widespread adoption, leaving many PV systems unmonitored. In contrast, we introduce a machine learning based technique that relies on satellite weather data and low-frequency inverter measurements for accurate fault diagnosis of PV systems. This allows one to adopt machine learning based fault diagnosis even for PV systems without on-site sensors. The proposed approach relies on a recurrent neural network to identify six relevant types of faults, based on the past 24 hours of measurements, as opposed to only taking into account the most recent measurement. Additionally, whereas state-of-the-art methods are limited to identifying the fault type, our model also estimates the output power reduction stemming from the fault, i.e., the fault severity. Comprehensive experiments on a simulated PV system demonstrate that this approach is sensitive to faults with a severity as small as 5%, reaching an accuracy of $96.9\% \pm 1.3\%$ using exact weather data and $86.4\% \pm 2.1\%$ using satellite weather data. Finally, we show that the model generalizes well to climates other than the climate of its training data and that the model is also able to detect unknown faults, i.e., faults that were not represented in the training data.

Keywords: Photovoltaics, Recurrent neural network, Time series classification, Fault diagnosis, Fault detection

1. Introduction

Solar energy has become a cornerstone in our efforts to mitigate climate change. According to the International Energy Agency, photovoltaic (PV) systems now offer the lowest electricity cost ever seen [1]. Consequently, the number of PV systems around the world is rapidly increasing [2]. With the growing interest in solar energy, the need for a cost-effective monitoring method for PV systems is apparent. Indeed, PV arrays are susceptible to many types of faults (e.g., short circuits or potential induced degradation (PID)), often caused by exposure to harsh weather [3]. The effects of faults in PV systems range from reduced power output and lifetime, to inverter failure and fire risk. Therefore, early fault detection is essential both to avoid power losses and to increase the efficiency and reliability of solar power generation.

Techniques for PV fault diagnosis can be broadly categorized as [3, 4, 5]:

- *Visual inspection*, which can identify browning, delamination, discoloration, partial shading, soiling, and cracked cells;

- *Infrared thermography*, suitable for diagnosing open and short circuits, delamination, partial shading, hot spots and PID;
- *Electrical methods*, which are able to identify various faults, including arc and grounding faults, PID and partial shading.

Both visual inspection by technicians and infrared thermography are not economical for small-scale PV systems. Therefore, the focus of this work is on electrical methods.

In the past decade, several automated fault diagnosis techniques for PV systems have been proposed. A common approach is to simulate the monitored PV system and compare the simulated power production with the real PV systems' observed output [6, 7, 8]. To reliably predict the power output of the PV system, the simulation requires weather measurements, such as irradiance and temperature. If the difference between the simulated and observed power output — also called the power residual — exceeds a fixed threshold, a fault is detected. For instance, Chouder and Silvester developed a technique that detects faults in PV systems via a threshold on the power residual [6]. Then, the detected fault is further distinguished into three categories (faulty string, faulty module or partial shading) by analyzing the ratios of the simulated and measured outputs. Drews et al. also detect faults by de-

*Corresponding author.

E-mail address: Jonas.VanGompel@UGent.be

terminating a threshold on the power residual, but obtain the irradiance and temperature data via weather satellites instead of relying on on-site sensors [7]. Although this reduces the sensitivity of the fault detection technique due to the larger error margin of weather data, it allows the technique to be implemented without requiring additional sensors. Once a fault is detected, the technique proposed in [7] determines whether the power reduction is constant or variable over time, but no further specification of fault type is provided. The method proposed by Garoudja et al. determines a threshold on the exponentially weighted moving average of the current, voltage and power residuals [8]. Hence, information of the residuals' history is included to detect faults, rather than only using the most recent observation.

Although PV fault diagnosis techniques based on thresholding are straightforward to implement and interpret, defining suitable values for the thresholds is challenging [9]. In particular, constructing optimal threshold rules to identify the fault type becomes increasingly complex as the number of considered input features and fault types grows. Furthermore, this approach lacks the flexibility to easily incorporate additional input features or fault types in an existing model. Machine learning based fault diagnosis offers a way to overcome these drawbacks. For instance, a hybrid method is proposed by Chine et al. which uses both thresholding and machine learning techniques to improve the model's fault classification capabilities [10]. Possible faults are again detected by defining a threshold on the power residual; however, the fault is now identified by combining a thresholding-based algorithm with an artificial neural network classifier. These algorithms rely on produced current and voltage, irradiance, PV module temperature and characteristics of the I-V curve to classify an impressive six types of faults. Unfortunately, this approach still requires a fixed threshold on the power residual. Moreover, the PV simulations providing the expected power output introduce an additional source of potential errors. Another hybrid approach is to obtain the residuals via Gaussian process regression [11] or principle component analysis [12], as opposed to using PV simulations. Although both these methods are able to automatically derive suitable thresholds for the residuals, they are limited to fault detection, meaning the type of the fault is not identified. Rather than comparing the expected and produced power output, Chen et al. manually engineer seven features from the I-V curve of the PV system [13]. Then, a kernel extreme learning machine (KELM) processes the extracted features to accurately predict the label of the PV system, defined as no fault, open circuit, short circuit, degradation or partial shading. Likewise, Spataru et al. manually define five features from the I-V curve, which are used as input for a set of fuzzy classifiers [14]. This method can identify degradation, partial shading and PID, which is rarely considered in electrical fault diagnosis techniques. Gao et al. propose a multi-grained cascade forest to detect partial shading, open and short circuit faults

without using weather data or I-V curves as inputs [15]. Instead, the technique relies on high-frequency current and voltage measurements to detect transient behaviour, indicating a fault has occurred. Similarly, Chen et al. employ a random forest to classify partial shading, degradation, open and short circuit faults using only high-frequency measurements of the operating voltage of the circuit and the current produced by each substring of the parallel circuit [16].

Existing machine learning based fault diagnosis techniques have shown promising results in terms of fault identification accuracy, but are not yet widely implemented in practice. The implementation is impeded by the costs associated with deploying on-site sensors and processing high-frequency measurements. In this work, these drawbacks are addressed by proposing a methodology that relies on weather satellite and inverter measurements with hourly resolution. These measurements are easier and cheaper to obtain, but provide less information than dedicated on-site sensors or high-frequency measurements. The resulting accuracy loss is partly counteracted by taking into account the temporal nature of the data: 24 hour windows of measurements are considered, as opposed to classifying single points in time. As recurrent neural networks are a natural choice for time series processing [17], a model based on stacked gated recurrent units (GRUs) is developed. The structure of the recurrent neural network and its training algorithm are described in [Section 4](#). In [Section 5](#), the performance of the proposed model is compared to that of CatBoost, which is a powerful machine learning algorithm based on gradient boosting of decision trees [18]. An overview of the proposed methodology is presented in [Section 2](#), while [Section 3](#) describes the considered faults and how they are simulated.

The main contributions of this paper are listed below.

- A stacked GRU neural network is developed to accurately detect and diagnose early occurrences of six faults common in PV systems.
- Aside from identifying the type of fault, the model also estimates its severity. Here, the severity of a fault refers to the average reduction in power output caused by the fault. Hence, the model is also able to detect unknown faults (i.e., faults which were not present in the training data), as the resulting reduction in power output is still detected.
- The proposed fault diagnosis technique is cost-effective and widely applicable, as its implementation does not require installation of additional sensors. Instead, weather satellite and inverter measurements with hourly resolution are used as inputs, whereas existing techniques often rely on dedicated on-site sensors or high-frequency measurements.

2. Recurrent neural network based fault diagnosis

The development of the machine learning model is divided in three phases: data collection, model training and testing of the trained model. In this work, a model based on recurrent neural networks is trained in a supervised setting, where the desired outputs for each input are known during training. For PV fault diagnosis, examples of desired outputs (also known as labels) are: no fault with 0% severity, short circuit with 10% severity, etc. Since large quantities of such labeled data are difficult to gather from PV arrays in the field, physics-based PV simulations are used to generate synthetic training data.

As visualized in Fig. 1, the input features of the model consist of the global horizontal irradiance and ambient temperature, the zenith angle of the sun, along with the current and voltage produced by the PV system. The irradiance and temperature are either obtained from weather satellite estimates or captured by on-site sensors, if these are available. Although using dedicated sensors increases the accuracy of the proposed methodology, this approach is more expensive to implement and maintain than using satellite weather data. The zenith angle of the sun can be easily inferred from the PV systems' location and time, while the current and voltage produced by the PV system are estimated via PV simulations, as described in Section 3. The five input features are all recorded with hourly resolution. These time series are fed into the recurrent neural network via a sliding window approach, where the model classifies each window of 24 hours as one of the seven considered types (see Fig. 1). Besides identifying potential faults, the model also provides an estimate of their severity.

3. Simulation of faults in photovoltaic systems

Training data for the model described in Section 4 is generated via a cell-level simulation based on the well-established single-diode model [19]. The physics-based PV simulation is detailed in [20] and has been experimentally validated by comparing the predicted and true energy yield of a residential PV system in Oldenburg, Germany [20, 21]. The mean absolute error (MAE) of the predicted energy yield is $3.6\% \pm 2.8\%$, where the reported error margin is the standard deviation. For comparison, the same task has been performed using the commercial PV simulation tool PVsyst [22], reaching a MAE of $5.5\% \pm 4.1\%$. Besides providing more accurate power output estimations than PVsyst, the PV simulation also predicts I-V curves which closely follow measured curves for various weather conditions [20]. These experiments demonstrate that the PV simulation described in [20] accurately models realistic PV systems [21]. Realistic weather inputs for the simulations are obtained from publicly available weather measurements from the database of the National Renewable Energy Laboratory [23]. These measurements are composed of the global horizontal irradiance, ambient

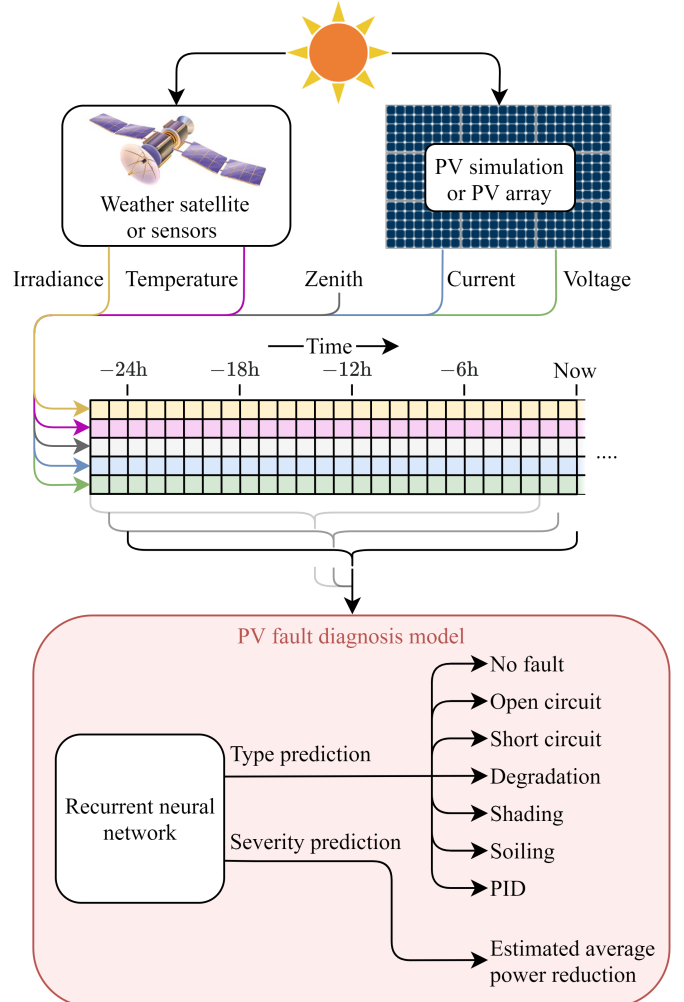


Figure 1: Summary of the proposed PV fault diagnosis method.

| Module parameter | Value |
|--------------------------------------------|---------------------|
| Number of cells (series \times parallel) | 24×3 |
| Maximum power point voltage | 37.7 V |
| Maximum power point current | 8.68 A |
| Series resistance | 0.448Ω |
| Shunt resistance | 263Ω |
| Open circuit voltage (V_{OC}) | 47.0 V |
| Short circuit current (I_{SC}) | 9.28 A |
| Temperature coefficient of V_{OC} | -146 mV/K |
| Temperature coefficient of I_{SC} | 4.08 mA/K |

Table 1: Characteristics of SW 325 XL duo modules.

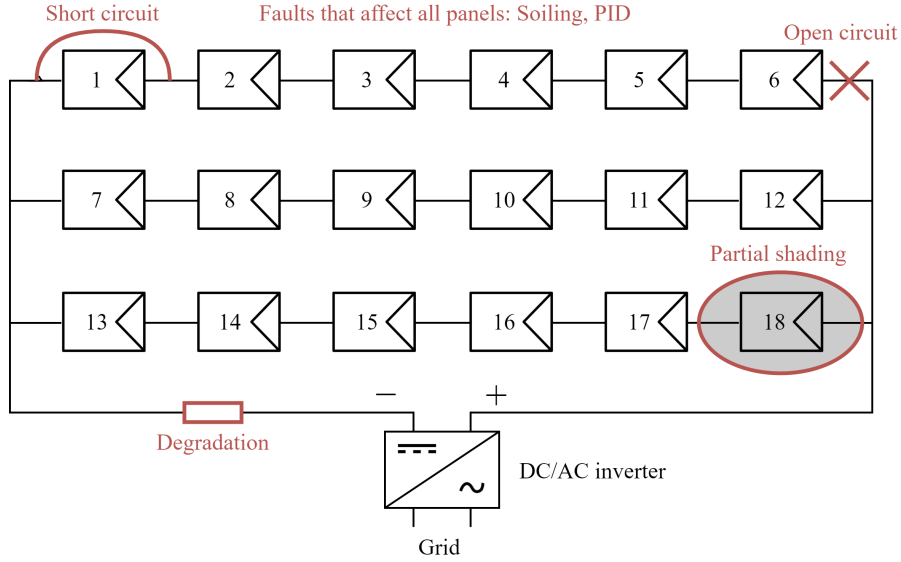


Figure 2: The considered PV system and faults, where individual modules have been numbered 1–18.

temperature, relative humidity, wind speed and wind direction during the period 19 November 2004 – 19 November 2014 at Elizabeth City State University, North Carolina.

To facilitate comparison with existing PV fault diagnosis methods, the same PV system is studied as in [13, 24]. This PV system consists of three parallel substrings of six panels in series, as shown in Fig. 2. The modules are facing the South and are tilted 35°. The specifications of the simulated PV modules are summarized in Table 1. The different faults affecting the PV system are also visualized in Fig. 2, while their causes and potential consequences are summarized in the following.

- The *open circuit* fault refers to a disconnection in the wiring of the PV system. This can be caused by a detached cable or melting due to a short circuit [8, 25]. Here, we consider two configurations, namely the disconnection of either one or two substrings.
- A *short circuit* in a PV system can affect PV cells, bypass diodes or entire modules. A short circuit between two points in the PV system that are at different potentials is known as a line-line fault, while a low resistance path between the ground and a point in the PV system is called a ground fault. The causes of short circuits are usually water ingress of PV modules or damaged cable insulation [4]. Possible effects of short circuits include energy losses, risk of fire and electric shock [25]. For this study, four severities of short circuits are simulated: short circuit of module 1, modules 1 and 2, modules 1–3 and lastly modules 1–4.
- The *degradation* or aging fault leads to an increase in the series resistance of the PV modules. Possible causes are mechanical stress, thermal cycling

and corrosion of connections in junction boxes, cables and solders [9]. Such degradation causes discontinuities in the conductors, which can lead to arc faults [25]. During an arc fault, a flow of current between conductors with significant voltage difference occurs, presenting a severe fire hazard. Following [13], degradation is simulated by setting the resistance of the resistor shown in Fig. 2 to 2Ω, 4Ω, 6Ω or 8Ω.

- *Partial shading* occurs when parts of the PV modules are exposed to less intense irradiance than the rest. Such shading can be cast by passing clouds, tall buildings, trees, chimneys or other obstacles. Shading by objects other than clouds is most prominent when the sun is low in the sky. Prolonged partial shading can lead to hot spots (i.e., local power dissipation caused by a reverse bias across PV cells) due to the difference in the I-V curves of shaded and non-shaded cells [4]. To simulate partial shading, we reduce the irradiance received by some modules when the sun is low in the sky, defined as the periods when the zenith angle of the sun is larger than 60°. Four severities of partial shading are considered by reducing the irradiance of:
 - module 18 by 50%,
 - module 18 by 50% and module 17 by 70%,
 - modules 18 and 12 by 50% and module 17 by 70%,
 - modules 18 and 12 by 50% and modules 17 and 11 by 70%.
- *Soiling* is the accumulation of dust and other light absorbing particles on the surface of PV modules,

giving rise to a reduction in produced current, an increase in module temperature and even hot spots [5]. Different severities of soiling are simulated by uniformly reducing the received irradiance of all modules by either 5%, 10%, 15% or 20%.

- *PID* originates from large voltage differences between crystalline silicon PV cells and the frame of the array [3]. Consequently, PID will be more prominent when many modules are connected in series. Here, we focus on the shunting type of PID, also known as PID-s, where electrochemical degradation caused by a voltage difference reduces the shunt resistance of the PV cells. This in turn gives rise to a leakage current between the cells and frame, severely reducing the power output. The PID-s simulation is described in [26]. We consider four severities of PID, corresponding to a 5%, 10%, 15% and 20% loss of average power output.

Early identification of these faults not only reduces power losses and increases the systems lifetime, but also prevents more serious consequences and their associated costs. In total, we simulate 23 configurations of the PV system in Fig. 2: no fault, two severities of open circuit and four severities of all other fault types. Note that it is important that multiple severities per fault type are included in the dataset; otherwise, the machine learning model might identify faults by simply recognizing their severity.

4. Model description

The goal of the machine learning model is to infer the type and severity of potential faults using 24 hourly measurements of global horizontal irradiance, ambient temperature, solar zenith angle and produced current and voltage. Neural networks possess the desired flexibility to simultaneously perform classification (fault identification) and regression (severity estimation). As the inputs of the neural network are multivariate time series, recurrent neural networks are especially suited for this task. Recurrent neural networks, such as long short-term memory (LSTM) and gated recurrent unit (GRU) networks, have been successfully applied to a wide range of tasks regarding sequential data, including speech recognition, machine translation and time series forecasting [17]. To minimize the computational requirements of the model, the first layers of the neural network can be shared for the classification and regression tasks. Following the above considerations, we developed a stacked GRU architecture to automatically extract features from the input time series. These features are then processed by two separate fully-connected layers, which perform the fault type classification and severity regression. A schematic representation is depicted in Fig. 3. The following subsections further detail the construction, training and testing of the model.

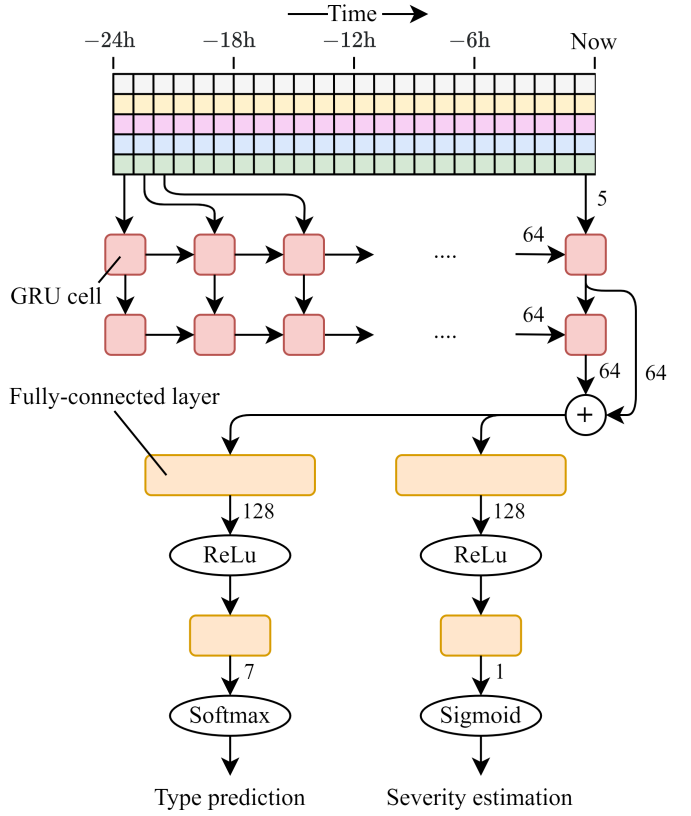


Figure 3: The proposed neural network. The numbers next to arrows indicate the dimension of the feature vectors that are passed.

4.1. Data preprocessing

In order to analyze different fault types and severities, 23 configurations of the PV system in Fig. 2 are considered, as discussed in Section 3. Each configuration is simulated for 10 years of publicly available weather measurements [23]. Due to missing measurements in the weather data, 12 days of the 10 years were removed. The shape of the dataset is therefore (3640, 23, 24, 5), corresponding to the number of days, configurations, hours in a day and input features, respectively.

To train and evaluate the model, the dataset is divided into a training, validation and test set. The validation set is used to monitor the generalization capabilities of the model during training (see Section 4.3). After the training is completed, the model is evaluated using the test set. The model's performance is extensively evaluated by performing 5-fold cross-validation. To this end, the order of the days in the dataset is randomly shuffled. The dataset is then divided into five subsets, of which four are used as training data. The remaining subset is further divided in two equal parts, which are the validation and test sets. During each of the five cross-validation iterations, a different subset is chosen as held-out data.

To ensure the methodology is applicable to a wide range of PV systems, the presence of dedicated voltage and current sensors is not assumed. Consequently, these input features will be measured by the inverter, which can

cause relative measurement errors of up to 5%. To mimic these errors, we add noise to the simulated current (I) and voltage (V) time series vectors as follows:

$$I' = (1 + U_1) \odot I$$

$$V' = (1 + U_2) \odot V.$$

Here, U_1 and U_2 are noise vectors of the same size as I and V , with elements drawn uniformly from the interval $[-0.05, 0.05]$. The symbol \odot denotes element-wise multiplication.

As neural networks are sensitive to magnitude differences in their input features, the data must be normalized before feeding it to the model. Input feature f is normalized by determining the mean $\mu_{f,\text{ok}}$ and standard deviation $\sigma_{f,\text{ok}}$ for the configuration without faults in the training set. Each measurement m in the time series of input feature f is then rescaled as

$$m' = \frac{m - \mu_{f,\text{ok}}}{\sigma_{f,\text{ok}}}.$$

Consequently, only the input features of the configuration without faults will have mean 0 and standard deviation 1. The reason we do not normalize each configuration separately, is that the relative scale of the current and voltage between the different configurations is essential information for the model. Note that the same $\mu_{f,\text{ok}}$ and $\sigma_{f,\text{ok}}$ (which are determined from the training set) are also used to rescale the validation and test sets.

Each hour, the model predicts the type and severity of a potential fault based on the past 24 hours, as indicated in Fig. 1. This sliding window approach enables the model to make hourly predictions, instead of having to wait 24 hours for an entire window of new measurements. Additionally, the sliding window acts as a form of data augmentation by increasing the number of training samples by a factor close to 24. Note that the sliding window is performed separately for each configuration, meaning no transitions between configurations are present in the data. A transition would be a sample with, for instance, the current and voltage during the first 23 hours originating from a system without faults, while the most recent measurement is from a system suffering from an open circuit. Ideally, we want the model to identify a fault as soon as it occurs, meaning the transition sample should be classified as open circuit. However, classifying transitions is significantly more challenging, as the model should decide to classify the transition sample as open circuit based solely on the most recent measurement. Hence, transition samples are not included in this study and should be considered for future work.

4.2. Loss function

Parameters of machine learning models are optimized by minimizing a suitable loss function. Since the model performs both classification (fault identification) and regression (severity estimation), its loss function consists of

| Symbol | Meaning |
|-------------------|---------------------------------------|
| α, β | Weights of the terms in \mathcal{L} |
| N | Number of training samples |
| w_i | Weight of sample i |
| c_i | True type of sample i |
| $\hat{y}_{c_i}^i$ | Softmax output of the model for c_i |
| s_i | True severity of sample i |
| \hat{s}_i | Predicted severity of sample i |

Table 2: Definition of the symbols used in Eq. (1).

a cross-entropy term and a mean squared error term [17]. Additionally, a third term is included which penalizes the model for predicting both no fault and a severity larger than zero at the same time, which is a contradictory output. The loss function is defined as follows

$$\mathcal{L} = \mathcal{L}_{\text{CE}} + \alpha \mathcal{L}_{\text{MSE}} + \beta \mathcal{L}_{\text{NFS}}$$

$$= \frac{1}{N} \sum_{i=1}^N w_i (\log \hat{y}_{c_i}^i + \alpha(s_i - \hat{s}_i)^2 + \beta \hat{s}_i \hat{y}_0^i), \quad (1)$$

where the symbols are defined in Table 2. A suitable relative weight of the terms in the loss function is obtained by setting $\alpha = 100$ and $\beta = 10$. The value of α is set as large as possible, up to the point where the classification performance of the model starts deteriorating. Similarly, β is set as small as possible, while still allowing the penalization term to prevent the model from simultaneously predicting no fault and a significant severity. The sample weights w_i are introduced to compensate for the class imbalance in the data: as described in Section 3, there is one configuration without faults, two configurations with open circuit faults and four configurations for all other faults. The sample weights are defined accordingly:

$$w_i = \begin{cases} 4 & \text{if } c_i = 0, \\ 2 & \text{if } c_i = 1, \\ 1 & \text{if } c_i > 1. \end{cases} \quad (2)$$

Here, type $c_i = 0$ is the configuration without faults, type $c_i = 1$ stands for the open circuit fault, and so on. The severity s_i of sample i is the reduction of the average power output caused by fault F_i (e.g., a short circuit of two PV modules). More specifically, s_i is defined as

$$s_i = 1 - \frac{P_{F_i}}{P_{\text{NF}}}, \quad (3)$$

where P_{NF} is the power produced by the system without faults, averaged over the set (train, validation or test) sample i belongs to. Similarly, P_{F_i} is the set's average of the power produced by the system suffering from fault F_i . For instance, if sample i is a training sample for the configuration with two modules in short circuit, then P_{NF} is the average produced power in the training set for the configuration without faults, while P_{F_i} is the average produced power in the training set for the configuration with two modules in short circuit.

4.3. Stacked GRU neural network

The proposed model is visualized in Fig. 3. First, two stacked GRU layers automatically extract features from the input sample. A GRU was chosen over an LSTM because it achieves similar performance with fewer parameters, and thus smaller computational requirements. Both GRU layers have a hidden dimension of 64 and are subject to recurrent dropout with a rate of 50%. After each GRU layer, layer normalization is applied to speed up training and to act as regularization [27]. As shown in Fig. 3, a residual connection over the second GRU layer is included to avoid vanishing gradients. The extracted features are then processed by two separate fully-connected layers with 128 nodes, followed by the ReLU activation [28]. Finally, the softmax activation [17] is applied to the output layer which classifies the type of the sample, while the sigmoid activation [17] is applied to the severity estimation output. The sigmoid is chosen because the predicted severity must lie in the interval $[0, 1]$.

The model is trained using a batch size of 128 and the Adam optimizer [29]. During training, the learning rate is reduced as the training progresses. The learning rate at optimization step t is given by

$$\gamma(t) = \frac{\gamma_0}{1 + \lambda t} = \frac{10^{-3}}{1 + 5 \cdot 10^{-5} t}.$$

To avoid overfitting, early stopping is employed. To this end, the model is evaluated on the validation set after every training epoch. Once training ends, the model is restored to the epoch where the highest balanced validation accuracy was achieved. Both the type prediction accuracy and the severity estimation MAE are balanced by weighing each sample i by w_i , as defined in Eq. (2).

4.4. Reference model: CatBoost

To compare the performance of the stacked GRU model, CatBoost is used as a reference. CatBoost uses a novel ordered gradient boosting approach to prevent overfitting [18]. Additionally, the algorithm employs symmetric decision trees to reduce its computational requirements. In contrast to the stacked GRU model, decision trees cannot perform classification and regression simultaneously, meaning two separate CatBoost models must be trained. Another consequence is that the penalization term described in Section 4.2 cannot be included in the loss function of the CatBoost models. Instead, the CatBoost fault type classifier minimizes the cross-entropy (see Eq. (1)), while the CatBoost regressor of the severity minimizes the root mean square error. Both losses are weighed by w_i , defined in Eq. (2). Since CatBoost does not take into account the temporal nature of the data, each input sample is first flattened from a $(24, 5)$ matrix to a vector of length 120. A grid search was performed to find optimal hyperparameters of the CatBoost classifier and regressor for the task at hand, however the default values of the implementation in [18] performed best, with the exception of *random_strength* of

the CatBoost classifier. This hyperparameter is set to 100 to prevent overfitting. As before, early stopping is used for both CatBoost models.

5. Results and discussion

Various experiments have been performed to verify the performance and robustness of our proposed technique. The stacked GRU and CatBoost models are tested in two application scenarios: with exact and satellite weather inputs. The term exact indicates that the machine learning model receives the same irradiance and temperature inputs as the PV simulation. In practice, this corresponds to the situation where accurate weather sensors are available on the PV installation site. Alternatively, the irradiance and temperature fed to the model are approximated by satellite data corresponding to the location of the PV system. This allows to explore the model’s ability to operate on PV systems without dedicated sensors. Furthermore, the model’s dependence on the climate of its training data is investigated by evaluating its performance on a test set originating from a different climate. Finally, we examine its ability to detect unknown faults using a threshold on the predicted severity.

5.1. Exact weather data

First, we consider the case where the model receives the same irradiance and temperature inputs as the PV simulation. As described in Section 4.1, inverter measurement errors are mimicked by adding 5% uniform noise to the current and voltage inputs of the model. After training, the model achieves a balanced classification accuracy of $96.9\% \pm 1.3\%$, which is the average over the test sets of the 5-fold cross-validation. The error margin is three times the standard deviation obtained from cross-validating. The accuracy is balanced by the sample weights w_i , as described in Section 4.3. More detailed classification results of the first cross-validation iteration are presented in the confusion matrix in Fig. 4, which shows that most mistakes are made when distinguishing between no fault and degradation.

The balanced MAE of the severity estimation is $0.67\% \pm 0.14\%$. The model predictions for the severity of the test samples after the first cross-validation iteration are shown in Fig. 5. Note that misclassified samples (orange dots) tend to coincide with a relatively poor severity estimation. This is not surprising, as both the fault classification and severity prediction rely on the same extracted features from the GRU layers. In Fig. 5, the effect of the penalization term in the loss function (see Eq. (1)) is apparent, especially for the configurations without faults and with degradation. For the samples without fault, a significant severity was only predicted when the sample was misclassified. Conversely, nearly zero severity was predicted for numerous degradation samples, as 6.2% of these were mistakenly classified as no fault (see Fig. 4). Unsurprisingly,

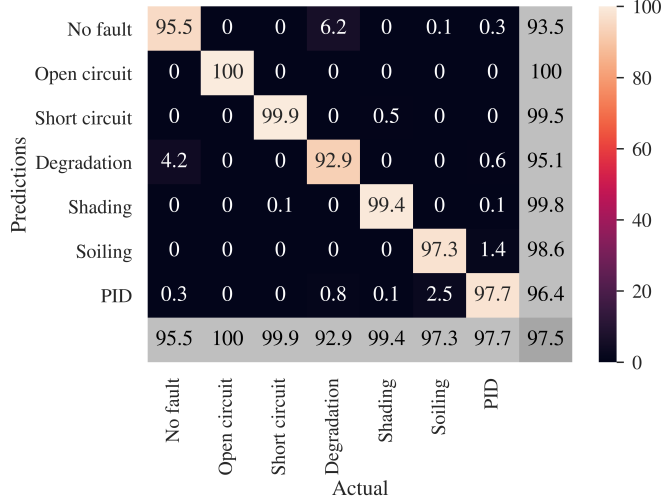


Figure 4: Stacked GRU’s classification accuracy percentages achieved on the test set using exact weather input. For each fault, the accuracy of all severity configurations are averaged. The grey column and row show the precision and recall, respectively.

most misclassifications occur for samples with low severity, as the effect of the fault is less discernible in these cases. Nevertheless, considering that the magnitude of the current and voltage noise is similar to the severity of some faulty configurations, the achieved balanced classification accuracy of $96.9\% \pm 1.3\%$ is remarkable. In Table 3, the results are compared to CatBoost. Note that, in contrast to the stacked GRU model, the CatBoost classifier and regressor are two separate models. Although all three models converged after training for a similar amount of time, stacked GRU outperforms CatBoost both in type classification and severity regression when exact weather data is used.

5.2. Test on different climate

One may wonder whether the climate of the weather measurements used for the training data should be similar to climate where the monitored PV system is located, or whether the trained model is general enough to be insensitive to the climate of its training data. To investigate this, an additional test set was created by running the simulations using weather measurements of the Edward Clark Generating Station in Nevada throughout the year 2014. These weather measurements are publicly available in the database of the National Renewable Energy Laboratory [23]. The model is still trained using 8 years of weather data from North Carolina, which has a humid subtropical climate, while it is now tested using weather data from the arid climate of Nevada. However, the results on the new test set are barely affected: the balanced classification accuracy and severity estimation MAE are now respectively $96.4\% \pm 1\%$ and $0.91\% \pm 0.12\%$. This demonstrates that the model generalizes well to different climates.

5.3. Satellite weather data

In order to explore the technique’s ability to operate without installed sensors, we use satellite estimates as irradiance and temperature input for the model. Note that the produced current and voltage are simulated using the weather measurements from the sensors, not from the satellite. Therefore, the current and voltage input for the model is the same as in the previous sections.

The freely available weather satellite data is obtained from MERRA-2 [30], which is spatially averaged over the entire state of North Carolina. As the satellite data is not specifically for the location of the Elizabeth City State University, where the weather sensors for the PV simulation are located, large deviations between the sensor and satellite data are observed. This is visualized in Fig. 6. The MAE between the sensor and satellite data is 49.9 W/m^2 for the irradiance and 2.39°C for the temperature. Note that for some hours, the irradiance estimated by the satellite is 850 W/m^2 higher than the sensory measurement. This severely complicates the PV fault diagnosis task, as measuring a lower power output than expected can be caused both by a fault or by the satellite overestimating the location specific irradiance. Additionally, a bias is observed for both measured input features: the satellite tends to overestimate the irradiance and underestimate the temperature. This is likely a consequence of the fact that the satellite data is for the entire state of North Carolina instead of the specific location of the sensors. The local nature of clouding explains why the irradiance deviations are larger than those of the temperature.

Despite the large error margins on the satellite data and 5% noise on the current and voltage, the model still reaches $86.4\% \pm 2.1\%$ balanced classification accuracy. Note that from the training data, the model can learn to take into account that the satellite’s irradiance estimates are highly noisy. This can explain the model’s relatively high test accuracy. The confusion matrix of the first cross-validation iteration in Fig. 7 shows that the model mostly has trouble distinguishing between no fault and soiling. This is because both an irradiance overestimation by the weather satellite and light absorption due to dust aggregation on the surface of the modules have similar effects: in both situations, the irradiance values given to the model are higher than what the modules actually receive.

The severity estimation of the test samples in the first cross-validation iteration is shown in Fig. 8. The balanced MAE of the severity estimation using satellite data is now of $2.09\% \pm 0.18\%$. Due to the uncertainty in irradiance, the severity of soiling tends to be underestimated by the model. This is also true for degradation and PID, albeit to a lesser degree. Nevertheless, the model is often still able to give a meaningful indication of the fault severity. As shown in the second row of Table 3, Stacked GRU also outperforms both CatBoost models when using satellite weather data.

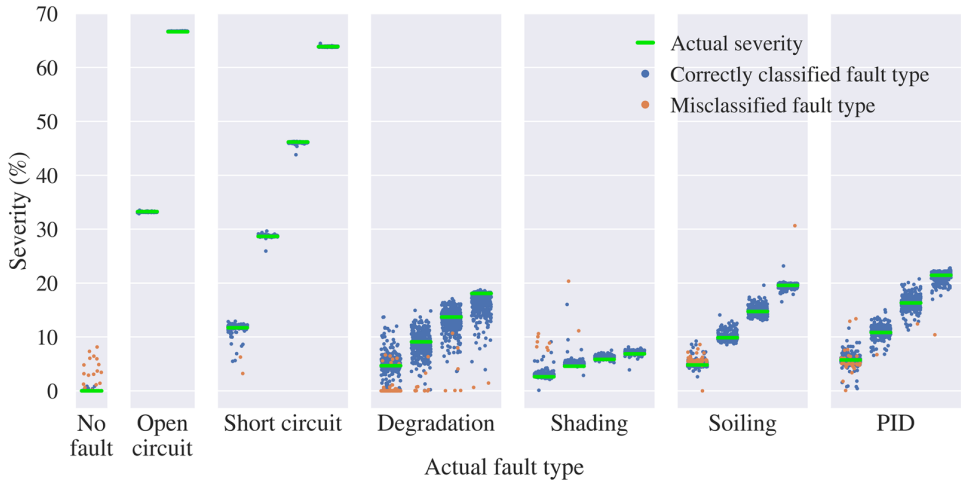


Figure 5: The true and predicted severity of the test samples, where the stacked GRU model used exact weather input. The green lines are the true severities, as defined in Eq. (3), while each dot is the model’s severity prediction for a sample. The fault type of the blue dots are correctly classified by the model, whereas the orange dots are misclassified. To avoid visual cluttering, only severity estimations of non-overlapping windows of 24 hours are shown.

| Weather data | Type prediction accuracy (%) | | Severity estimation MAE (%) | |
|--------------|------------------------------|----------------|-----------------------------|-----------------|
| | CatBoost classifier | Stacked GRU | CatBoost regressor | Stacked GRU |
| Exact | 93.2 ± 1.3 | 96.9 ± 1.3 | 1.66 ± 0.12 | 0.67 ± 0.14 |
| Satellite | 83.5 ± 2.1 | 86.4 ± 2.1 | 3.6 ± 0.24 | 2.09 ± 0.18 |

Table 3: The 5-fold cross-validation results of the balanced accuracy and MAE reached by the models. All models were trained for a similar amount of time. The error margins are three times the standard deviations obtained from 5-fold cross-validation.

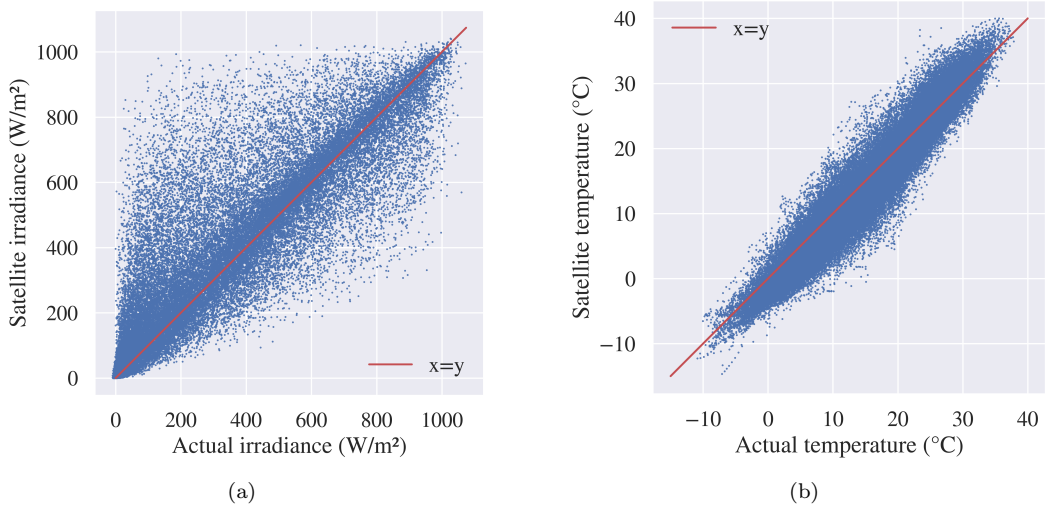


Figure 6: Comparison of the irradiance (a) and temperature (b) measurements originating from either the on-site sensors or a weather satellite. The x-value of each dot represents the sensory measurement for that hour, while the y-value is the satellite estimate. Ideally, for each hour, the satellite estimate would be equal to the measurement. This would mean that all dots lie on the red $x = y$ line.

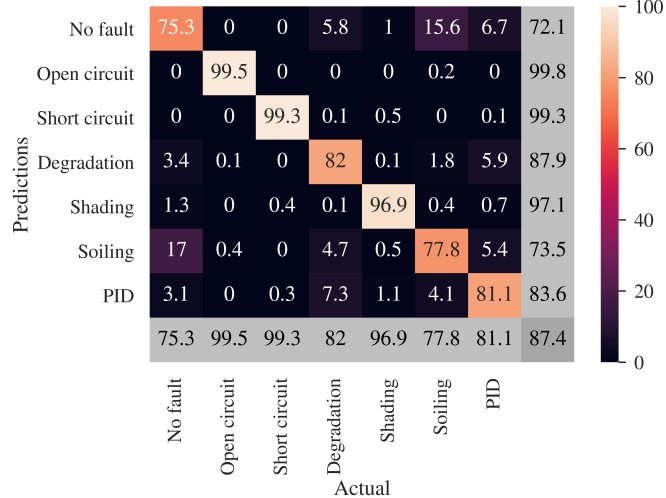


Figure 7: Stacked GRU’s classification accuracy percentages achieved on the test set using satellite weather input. The grey column and row show the precision and recall, respectively.

5.4. Test on unknown faults

The severity estimation capability of the model can be exploited to detect unknown faults. An unknown fault is a type of fault that is not represented in the training data, which poses a challenge to existing PV fault diagnosis classifiers [13, 15, 16]. By defining a threshold on the predicted severity, our model is able to detect such unknown faults. In contrast to the previous sections, this is a binary classification problem: a sample is classified either as faulty or as not faulty.

As a proof of concept, the threshold is defined simply as the maximum severity predicted for correctly classified samples without faults in the validation set. Figure 9 shows the predicted severities in the test set using exact weather data, where all PID samples were excluded from the train and validation sets. As the model is not trained to identify PID, all PID samples in the test set are misclassified. Nevertheless, 97.5% of the PID test samples have a predicted severity larger than the threshold and are therefore detected as a fault. By repeating this procedure, each time excluding a different fault, we obtain the detection accuracies reported in the first row of Table 4. This results in an unknown fault detection accuracy, averaged over the six fault types, of 94.3%. As the model needs to be retrained for every case considered in Table 4, these results were not cross-validated. When detecting degradation as an unknown fault, the accuracy is significantly lower compared to other faults. This is likely related to the fact that the model trained on all faults confuses no fault and degradation relatively often, as shown in Fig. 4.

When using satellite weather data, the detection accuracy for soiling drops significantly, while an increase in accuracy is observed for degradation (see Table 4). This behaviour can be understood by comparing Fig. 4 and Fig. 7: with satellite weather data, notably more misclassifi-

cations occur when distinguishing between no fault and soiling, while degradation and no fault samples are confused with each other less often. Overall, the unknown fault detection accuracy is now 80.4%.

6. Conclusions and outlook

A model based on gated recurrent units (GRUs) is proposed to accurately identify six common faults in photovoltaic (PV) installations. By considering 24 hour windows of measurements, as opposed to single points in time, our technique is able to operate without I-V curve tracers, high-frequency measurements or weather sensors, which are often required for state-of-the-art fault diagnosis methods. Rather, weather satellite and inverter measurements are used as inputs for the stacked GRU model. Our technique is sensitive to faults with a severity (i.e., average power output reduction) as small as 5%. Furthermore, the model estimates the severity of the fault on top of the classification, whereas the state-of-the-art is mostly limited to fault classification. Besides providing useful information for maintenance purposes, the severity estimation also allows the model to detect unknown faults by observing the resulting reduction in power output.

Interesting future research directions include the classification of multiple faults occurring simultaneously and the incorporation of transitions in the training data, where for example the first hours of an input time series are from a system without faults, while for later hours a short circuit is present. Training on such transitions would allow the model to react more quickly to the occurrence of a fault, which is particularly interesting for real-time monitoring of PV arrays. Another possibility is to further improve the model’s performance by increasing the time resolution or input window size, at the cost of higher computational requirements. Finally, the model will be tested experimentally by monitoring PV arrays in the field which suffer from known faults.

Acknowledgements

This work was supported by the DAPPER project, which is financed by Flux50 and Flanders Innovation & Entrepreneurship (project number HBC.2020.2144). We would like to thank Arnaud Schils for facilitating the PV simulations.

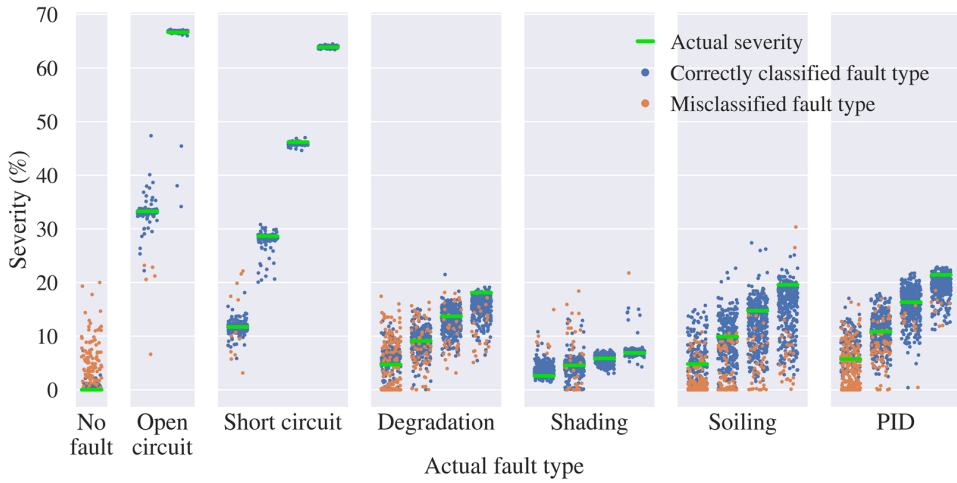


Figure 8: The true and predicted severity of the test samples, where the stacked GRU model used satellite weather inputs.

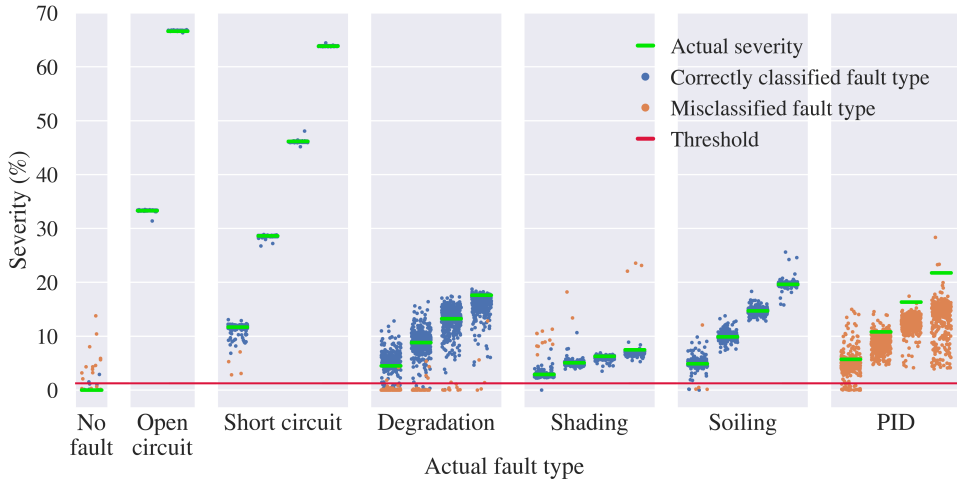


Figure 9: The true and predicted severity of the test samples, where the stacked GRU model used exact weather input. PID samples were excluded from the training and validation sets of this model. The red line represents the severity threshold above which samples are detected as faulty. Although the fault type predictions of the unknown fault samples are incorrect, 97.5% of the PID samples have a predicted severity larger than the threshold and are therefore detected as faulty.

| Weather data | Detection accuracy of excluded fault (%) | | | | | | |
|--------------|------------------------------------------|---------------|-------------|---------|---------|------|-------------|
| | Open circuit | Short circuit | Degradation | Shading | Soiling | PID | Average (%) |
| Exact | 100 | 99.6 | 70.7 | 98.4 | 99.7 | 97.5 | 94.3 |
| Satellite | 100 | 98.4 | 83.4 | 93 | 22.3 | 85.2 | 80.4 |

Table 4: Threshold detection accuracy of each fault that was excluded from the training and validation sets.

References

- [1] IEA (2020), "World energy outlook 2020." <https://www.iea.org/reports/world-energy-outlook-2020>.
- [2] SolarPower Europe, *Global market outlook for solar power 2018-2022*. Tech. rep. Bruxelles: European Photovoltaic Industry Association, 2018.
- [3] M. Koentges, S. Kurtz, C. Packard, U. Jahn, K. A. Berger, K. Kato, *et al.*, *Review of failures of photovoltaic modules*. IEA International Energy Agency, 2014.
- [4] A. Mellit, G. M. Tina, and S. A. Kalogirou, "Fault detection and diagnosis methods for photovoltaic systems: A review," *Renewable and Sustainable Energy Reviews*, vol. 91, pp. 1–17, 2018.
- [5] A. Livera, M. Theristis, G. Makrides, and G. E. Georghiou, "Recent advances in failure diagnosis techniques based on performance data analysis for grid-connected photovoltaic systems," *Renewable energy*, vol. 133, pp. 126–143, 2019.
- [6] A. Chouder and S. Silvestre, "Automatic supervision and fault detection of PV systems based on power losses analysis," *Energy conversion and Management*, vol. 51, no. 10, pp. 1929–1937, 2010.
- [7] A. Drews, A. De Keizer, H. G. Beyer, E. Lorenz, J. Betcke, W. Van Sark, *et al.*, "Monitoring and remote failure detection of grid-connected PV systems based on satellite observations," *Solar energy*, vol. 81, no. 4, pp. 548–564, 2007.
- [8] E. Garoudja, F. Harrou, Y. Sun, K. Kara, A. Chouder, and S. Silvestre, "Statistical fault detection in photovoltaic systems," *Solar Energy*, vol. 150, pp. 485–499, 2017.
- [9] D. S. Pillai and N. Rajasekar, "A comprehensive review on protection challenges and fault diagnosis in PV systems," *Renewable and Sustainable Energy Reviews*, vol. 91, pp. 18–40, 2018.
- [10] W. Chine, A. Mellit, V. Lugh, A. Malek, G. Sulligoi, and A. M. Pavan, "A novel fault diagnosis technique for photovoltaic systems based on artificial neural networks," *Renewable Energy*, vol. 90, pp. 501–512, 2016.
- [11] R. Fazai, K. Abodayeh, M. Mansouri, M. Trabelsi, H. Nounou, M. Nounou, *et al.*, "Machine learning-based statistical testing hypothesis for fault detection in photovoltaic systems," *Solar Energy*, vol. 190, pp. 405–413, 2019.
- [12] B. Taghezouit, F. Harrou, Y. Sun, A. H. Arab, and C. Larbes, "Multivariate statistical monitoring of photovoltaic plant operation," *Energy Conversion and Management*, vol. 205, p. 112317, 2020.
- [13] Z. Chen, L. Wu, S. Cheng, P. Lin, Y. Wu, and W. Lin, "Intelligent fault diagnosis of photovoltaic arrays based on optimized kernel extreme learning machine and IV characteristics," *Applied Energy*, vol. 204, pp. 912–931, 2017.
- [14] S. Spataru, D. Sera, T. Kerekes, and R. Teodorescu, "Diagnostic method for photovoltaic systems based on light I–V measurements," *Solar Energy*, vol. 119, pp. 29–44, 2015.
- [15] W. Gao, R.-J. Wai, and S.-Q. Chen, "Novel PV fault diagnoses via SAE and improved multi-grained cascade forest with string voltage and currents measures," *IEEE Access*, vol. 8, pp. 133144–133160, 2020.
- [16] Z. Chen, F. Han, L. Wu, J. Yu, S. Cheng, P. Lin, *et al.*, "Random forest based intelligent fault diagnosis for PV arrays using array voltage and string currents," *Energy conversion and management*, vol. 178, pp. 250–264, 2018.
- [17] I. Goodfellow, Y. Bengio, A. Courville, and Y. Bengio, *Deep learning*, vol. 1. MIT press Cambridge, 2016.
- [18] L. Prokhorenkova, G. Gusev, A. Vorobev, A. V. Dorogush, and A. Gulin, "Catboost: unbiased boosting with categorical features," in *Advances in Neural Information Processing Systems*, vol. 31, Curran Associates, Inc., 2018.
- [19] N. Pearsall, *The performance of photovoltaic (PV) systems: modelling, measurement and assessment*. Woodhead Publishing, 2016.
- [20] H. Goverde, B. Herteleer, D. Anagnostos, G. Köse, D. Goossens, B. Aldaladi, *et al.*, "Energy yield prediction model for pv modules including spatial and temporal effects," in *European Photovoltaic Solar Energy Conference and Exhibition*, 2014.
- [21] D. Anagnostos, H. Goverde, B. Herteleer, F. Catthoor, S. Dimitrios, J. Driesen, *et al.*, "Demonstration and validation of an energy yield prediction model suitable for non-steady state non-uniform conditions," in *The 6th World Conference on Photovoltaic Energy Conversion*, 2014.
- [22] A. Mermoud, C. Rocker, and J. Bonvin, "Pvsyst (version 6.23)," *Computer Software*. Geneva, Switzerland: ISE, University of Geneva. Retrieved May, vol. 1, p. 2014, 1994.
- [23] A. Andreas and T. Stoffel, "Elizabeth City State University: Elizabeth City, North Carolina (data)." NREL Report No. DA-5500-56517, 1985. <http://dx.doi.org/10.5439/1052558>.
- [24] A. Y. Appiah, X. Zhang, B. B. K. Ayawli, and F. Kyeremeh, "Long short-term memory networks based automatic feature extraction for photovoltaic array fault diagnosis," *IEEE Access*, vol. 7, pp. 30089–30101, 2019.
- [25] M. K. Alam, F. Khan, J. Johnson, and J. Flicker, "A comprehensive review of catastrophic faults in PV arrays: types, detection, and mitigation techniques," *IEEE Journal of Photovoltaics*, vol. 5, no. 3, pp. 982–997, 2015.
- [26] A. Schils, J. Carolus, J. Ascencio-Vásquez, A. Wabbes, E. Bertrand, M. Daenen, *et al.*, "A grey box model for shunting-type potential induced degradation in silicon photovoltaic cells under environmental stress," to be published in *EU PVSEC 2021*.
- [27] J. L. Ba, J. R. Kiros, and G. E. Hinton, "Layer normalization," *arXiv preprint arXiv:1607.06450*, 2016.
- [28] V. Nair and G. E. Hinton, "Rectified linear units improve restricted boltzmann machines," in *Icmi*, 2010.
- [29] D. P. Kingma and J. Ba, "Adam: A method for stochastic optimization," *arXiv preprint arXiv:1412.6980*, 2014.
- [30] R. Gelaro, W. McCarty, M. J. Suárez, R. Todling, A. Molod, L. Takacs, *et al.*, "The modern-era retrospective analysis for research and applications, version 2 (MERRA-2)," *Journal of climate*, vol. 30, no. 14, pp. 5419–5454, 2017. <https://www.renewables.ninja/>.